TU Delft

Delft University of Technology

Electrical characteristics and photodetection mechanism of TiO_2/AlGaN/GaN heterostructure-based ultraviolet detectors with a Schottky junction

Zhan, Teng; Sun, Jianwen; Feng, Tao; Zhang, Yulong; Zhou, Binru; Zhang, Banghong; Wang, Junxi; Sarro, Pasqualina M.; Zhang, Guoqi; More Authors

DOI
10.1039/d2tc04491a

Publication date
2022

Document Version
Final published version

Published in
Journal of Materials Chemistry C

Citation (APA)
Zhan, T., Sun, J., Feng, T., Zhang, Y., Zhou, B., Zhang, B., Wang, J., Sarro, P. M., Zhang, G., & More Authors (2022). Electrical characteristics and photodetection mechanism of TiO_2/AlGaN/GaN heterostructure-based ultraviolet detectors with a Schottky junction. *Journal of Materials Chemistry C*, *11 (2023)*(5), 1704-1713. https://doi.org/10.1039/d2tc04491a

Important note
To cite this publication, please use the final published version (if applicable).
Please check the document version above.

Copyright
Other than for strictly personal use, it is not permitted to download, forward or distribute the text or part of it, without the consent of the author(s) and/or copyright holder(s), unless the work is under an open content license such as Creative Commons.

Takedown policy
Please contact us and provide details if you believe this document breaches copyrights.
We will remove access to the work immediately and investigate your claim.

This work is downloaded from Delft University of Technology.
For technical reasons the number of authors shown on this cover page is limited to a maximum of 10.

Green Open Access added to TU Delft Institutional Repository

'You share, we take care!' - Taverne project

https://www.openaccess.nl/en/you-share-we-take-care

Otherwise as indicated in the copyright section: the publisher
is the copyright holder of this work and the author uses the
Dutch legislation to make this work public.

Published on 13 December 2022. Downloaded by Technische Universiteit Delft on 1/17/2023 8:23:20 AM.

Journal of
Materials Chemistry C

ROYAL SOCIETY OF CHEMISTRY

PAPER

View Article Online
View Journal

Cite this: DOI: 10.1039/d2tc04491a

Electrical characteristics and photodetection mechanism of TiO_2/AlGaN/GaN heterostructure-based ultraviolet detectors with a Schottky junction†

Teng Zhan, ‡[ac] Jianwen Sun,‡[b] Tao Feng,[ac] Yulong Zhang,[b] Binru Zhou,[ac] Banghong Zhang,[ac] Junxi Wang,[ac] Pasqualina M. Sarro,[d] Guoqi Zhang,[d] Zewen Liu,*[b] Xiaoyan Yi*[ac] and Jinmin Li*[ac]

Received 22nd October 2022,
Accepted 12th December 2022

DOI: 10.1039/d2tc04491a

rsc.li/materials-c

Recent research focusing on wide-bandgap and two-dimensional materials with a Schottky junction has provided a new concept for ultraviolet photodetectors. However, the working mechanism of the Schottky junction-based detector varies depending on the photosensitive materials used and the device structure. We demonstrated a TiO_2/AlGaN/GaN heterostructure-based photodetector with a Schottky junction, integrating an ultraviolet photosensitive TiO_2 nanolayer, a two-dimensional electron gas (2DEG) field effect transistor, and a metal–semiconductor Schottky diode. The spectral response wavelength region of the detector is 200–365 nm and the peak responsivity is 37.396 A W^{-1} at −5 V bias under 240 nm UV illumination, respectively. Meanwhile, a peak photo-to-dark current ratio (PDCR) of 5.1 × 10^2 at −2 V bias voltage was observed under 274 nm UV irradiation. This Schottky-based 2DEG heterostructure detector can realize three dominant working principles: (i) the Schottky emission mechanism at a low reverse voltage (0–1 V) before the current is fully turned on, (ii) the Poole-Frenkel emission mechanism at a medium reverse voltage (−1 to −2 V) with peak PDCR, and (iii) the Fowler-Nordheim tunneling mechanism at a high reverse voltage (> −2 V) with a high responsivity. Continuous cycle response measurement results indicate that the detectors have good response repeatability and reliability. The characteristics of response wavelength, responsivity, and stability show that the detector can be used for several commercial applications, including sunscreen UV monitoring and LED sterilization light source detection.

Introduction

Ultraviolet (UV) light is electromagnetic radiation with wavelengths ranging from 100 to 400 nm, and can be divided into three ranges: UVC, UVB, and UVA, with corresponding wavelengths of 100–280 nm, 280–315 nm, and 315–400 nm, respectively. Ozone levels around the earth block different bands of ultraviolet radiation. UVA is hardly affected by the ozone, and most of it reaches the earth's surface. However, UVC is strongly absorbed by the ozone layer and the atmosphere, whereas UVB is mostly absorbed by the ozone layer. Solar-blind region irradiation is almost nonexistent in the atmosphere near the ground. Hence, UV light detectors have several applications in different fields owing to their distribution and characteristics. Applications for UVC or solar-blind regions are mostly limited to specialized fields such as LED sterilization light source monitoring, missile or rocket warning, and non-line-of-sight optical communication. For UVB and UVA regions, applications cover consumer and industrial fields, such as sunscreen UV detection and ultraviolet curing light source monitoring.[1–4]

The performance of an ultraviolet detector is usually dependent on the bandgap of photosensitive materials and the device structure.[5] Many ultrawide bandgap semiconductors, including high-aluminum-content gallium nitride (AlGaN, 4.4–5.1 eV),[6–8] aluminum nitride (AlN, 6.2 eV),[1,9] gallium oxide (Ga_2O_3, 4.4–5.3 eV),[10–14] and boron nitride (BN, 4.5–5.5 eV), have been

[a] Research and Development Center for Solid State Lighting, Institute of Semiconductors, Chinese Academy of Sciences, Qinghua East Road 35A, 100083, Beijing, China. E-mail: spring@semi.ac.cn, jmli@semi.ac.cn
[b] School of Integrated Circuits, Tsinghua University, 100084, Beijing, China. E-mail: liuzw@tsinghua.edu.cn
[c] College of Materials Sciences and Opto-Electronic Technology, University of Chinese Academy of Sciences, No. 19A Yuquan Road, Beijing, 100049, China
[d] Department of Microelectronics, Delft University of Technology, 2628 CD Delft, The Netherlands

† Electronic supplementary information (ESI) available. See DOI: https://doi.org/10.1039/d2tc04491a

‡ Teng Zhan and Jianwen Sun contributed equally to this work.

Published on 13 December 2022. Downloaded by Technische Universiteit Delft on 1/17/2023 8:23:20 AM.

widely used in UV detection technology.[15,16] Owing to the characteristics of oxygen molecule adsorption and UV absorption, many wide-bandgap metal oxide materials, including zinc oxide (ZnO, 3.29 eV),[17,18] tungsten oxide (WO_3, 2.6 eV),[19–22] stannic oxide (SnO_2, 3.8 eV),[23,24] and titanium oxide (TiO_2, 3.2 eV),[25,26] have also been extensively studied. Based on the different working principles, the UV semiconductor detector structures can be classified into the following types: Schottky barrier photodiodes,[27] photoconductors,[28] p–n or p–i–n junction types[29] and field-effect transistor-based structures.[22,30]

The Schottky-contact structure-based detector can show excellent performance in photoelectric response parameters owing to the energy band and various working mechanisms in the Schottky junction. Many device fabrication methods and materials based on the Schottky junction have been reported. Hu *et al.* presented an important concept of using the Schottky contact to achieve super sensitive and fast response ZnO nanowire-based nanosensors.[30] Luo *et al.* demonstrated a high responsivity graphene/single GaAs nanowire Schottky junction photovoltaic device with a short response/recovery time.[31] Zhang *et al.* developed a flexible piezoelectric strain sensor based on an indium-doped ZnO nanobelt with a Schottky barrier.[32] Shen *et al.* proposed a high-performance Schottky junction device with electrodes from directly grown graphene nanowalls.[33] Jiang *et al.* demonstrated a hybrid heterostructure with an ultrathin vanadium dioxide film and molybdenum ditelluride nanoflakes with a Schottky junction mode.[34] Meanwhile, researchers thoroughly investigated the current conduction mechanisms of their Schottky junction-based devices, including Schottky emission (SE) or thermal emission (TE), thermionic-field emission (TFE), tap-assisted tunneling (TAT), hopping conduction, Poole–Frenkel (PF) emission, and Fowler–Nordheim (FN) tunneling. Xu *et al.* systematically explained the TEF and FN tunneling mechanisms at different electric field injection regions of the Ga_2O_3 film-based Schottky solar-blind photodetectors.[35] Wang *et al.* discussed the TE mechanism and temperature-dependent rectifying characteristics of the ZnSe nanowire detector with Schottky barrier diodes.[36] Fan *et al.* found that when thin film capacitors are driven at low and high electric fields, the working mechanism shifts from bulk-limited ohmic to FN tunneling or SE.[37]

This research demonstrates a novel type of TiO_2/AlGaN/GaN heterostructure-based photodetector with a Schottky junction, which integrates a 2DEG field-effect transistor and a metal-semiconductor Schottky junction. The characteristics and working mechanisms are illustrated and discussed in the Results and discussion section. A TiO_2 photosensitive nanolayer was deposited at the gate area of an AlGaN/GaN 2DEG epitaxial heterostructure *via* magnetron sputtering. A Ti/Au layer stack was evaporated to form a Schottky contact with AlGaN epitaxial materials in the source electrode area. Owing to the various current conduction mechanisms of the Schottky barrier, the peak responsivity and a photo-to-dark current radio (PDCR) of the detector were 37.396 A W^{-1} at −5 V bias under 240 nm illumination and 5.1×10^2 at −2 V bias under 274 nm UV illumination, respectively. The sharp cutoff wavelength was located at 365 nm. The characteristics of the TiO_2 photosensitive layer and AlGaN epilayer indicate that the device can be used for sunscreen UV monitoring and LED sterilization light source detection.

Experimental

Epitaxy growth and chip fabrication

The AlGaN/GaN epitaxial heterostructure was grown on a 1 mm thick ⟨111⟩ silicon substrate wafer using the metal-organic chemical vapor deposition technique. An undoped GaN buffer layer (4.7 μm), followed by a GaN channel layer (300 nm), an AlN interlayer (1 nm), an undoped Al0.22Ga0.78N barrier layer (21 nm), and a GaN cap layer (2 nm), was deposited. The electron mobility of the 2DEG was $\sim$1500 $cm^2\ V^{-1}\ s^{-1}$, with a sheet electron density of $\sim 1 \times 10^{13}\ cm^{-3}$. The chip fabrication started with mesa etching to define the active area. Then, a Ti/Al/Ti/Au (20/110/40/50 nm) ohmic metallization multilayer film was deposited *via* electron beam evaporation and patterned by lift-off (LLO) methods. After patterning, the ohmic contact was annealed at 870° for 45 s under ambient N2. Next, an evaporated Ti/Pt (30/200 nm) was patterned by LLO to form the microheater, followed by a 200 nm SiO_2 layer for isolation from the interconnect layer *via* plasma-enhanced chemical vapor deposition (PECVD). The evaporated Ti/Au (20/300 nm) layer stack was used to form a Schottky contact. The topside of the wafer was passivated with a 200 nm PECVD SiO_2 layer and etched in buffered oxide etch solution to open the contact pads and gate windows. A 10 nm TiO_2 nanolayer was deposited on the AlGaN/GaN heterostructure surface to form the ultraviolet (UV) photosensitive floating gate *via* magnetron sputtering. The silicon substrate was polished down to 400 μm from the backside and etched by deep reactive ion etching to form a circular membrane with a diameter of 600 μm in the final step. After dicing, the 1 mm × 1 mm single chip was packaged into a TO-46 socket with a quartz window and in an N_2 atmosphere, as shown in Fig. S1 (ESI†).

Detection measurements and analysis instruments

To analyze the properties of the TiO_2 nanolayer and the performances of the fabricated devices, some measurements were performed. An ultraviolet-visible spectrophotometer (Hitachi, UH4150) was used to obtain the absorption spectrum of the TiO_2 nanolayer. The structures of the devices were visualized using SEM (Hitachi, S-4800). The spectral response of the TiO_2/AlGaN/GaN Schottky photodetectors was measured using a spectrometer testing DSR200 system (Zolix Instrument Co., Ltd, China), which includes a power supply, a chopper wheel, a beam mirror, and a 150 W xenon lamp. The current–voltage (*I*–*V*) and current–time (*I*–*t*) values were measured in the dark or under the illumination of a 274 nm UVC LED (Advanced Ultraviolet Optoelectronics Co., Ltd, China) using a Keithley source meter 2420. The light intensity of the UVC LED was measured using a spectroradiometer system (JETI Technische Instrumente GmbH, specbos 1211UV, Germany). All the electrical

 This journal is © The Royal Society of Chemistry 2023

Published on 13 December 2022. Downloaded by Technische Universiteit Delft on 1/17/2023 8:23:20 AM.

and photoelectric response results of the detector were measured at room temperature (300 K).

Results and discussion

Fig. 1(a) shows the schematic of the TiO_2/AlGaN/GaN heterostructure photodetector with the Schottky junction. Fig. S2 (ESI†) presents a cross-section schematic diagram of the device. TiO_2 is an n-type ultraviolet and gas photosensitive semiconductor. The adsorption of oxygen molecules from the air and ultraviolet absorption from light illumination can alter the surface charges and states of the TiO_2 nanolayer, thereby disrupting the gate potential and AlGaN/GaN 2DEG channel concentration. All of these can be regarded as a photosensitive floating gate effect on the 2DEG channel of the AlGaN/GaN heterostructure, and the device model is illustrated in Fig. 1(a). The inset of Fig. 1(a) illustrates the device model of a 2DEG FET and a Schottky diode, one is the AlGaN/GaN heterostructure and the other is the Ti/AlGaN Schottky contact. Fig. 1(b) presents the energy dispersive spectroscopy (EDS) spectra of the gate area of the device for a binding energy range from 0 KeV to 7 KeV. The percentage of Ti, O, Ga, N and Al is 0.5%, 6.24%, 53.51%, 39.62% and 0.13%, respectively. The inset of Fig. 1(b) shows the SEM image of the detector and the elemental distribution of the gate area, and the distribution of each element is dense. Fig. S1 (ESI†) shows the optical image of the complete TiO_2/AlGaN/GaN heterostructure photodetector with a chip size of 1 mm × 1 mm and an active area of 340 μm × 340 μm, which was packaged into a TO-46 socket by 50 μm thick Au wires *via* wire bonding in a nitrogen atmosphere. Fig. 1(c) shows the absorption spectrum of the 10 nm TiO_2 nanolayer. The TiO_2 nanolayer has a cutoff wavelength edge of 365 nm, which covers the range of UVB and UVC light. Based on the relationship between the absorption value and bandgap, the function curve of $(\alpha h\nu)^2$ concerning $h\nu$ is shown in the inset of Fig. 1(c), where the bandgap of this 10 nm TiO_2 film is calculated to be 3.9 eV. Fig. 2(d) presents the *I–V* characteristics of the TiO_2/AlGaN/GaN UV detector in a dark state and under 274 nm UV light irradiation with a light intensity of 504.2 μW cm^{-2}. The scanning bias voltage ranged from −5 V to 4 V and there was a significant response current when the detector was operated under both forward and reverse bias voltages. For example, under 274 nm UV illumination with an intensity of 504.2 μW cm^{-2} at a reverse bias of 3 V, the dark current and the UV illumination photocurrent of the photodetector were 3.44 mA and 15.54 mA, respectively. Under −1 V bias, the dark current and photocurrent were 1.836 nA and 39.543 nA, respectively. Under −5 V bias, the dark current and the photocurrent were 0.332 μA and 18.514 μA, respectively. Fig. 1(e) shows the spectral response of the detector at −5 V bias indicating high responsivity in the UV region (wavelength of 200–365 nm). The photodetector with a Schottky contact had a peak responsivity of 37.396 A W^{-1} at −5 V bias voltage under

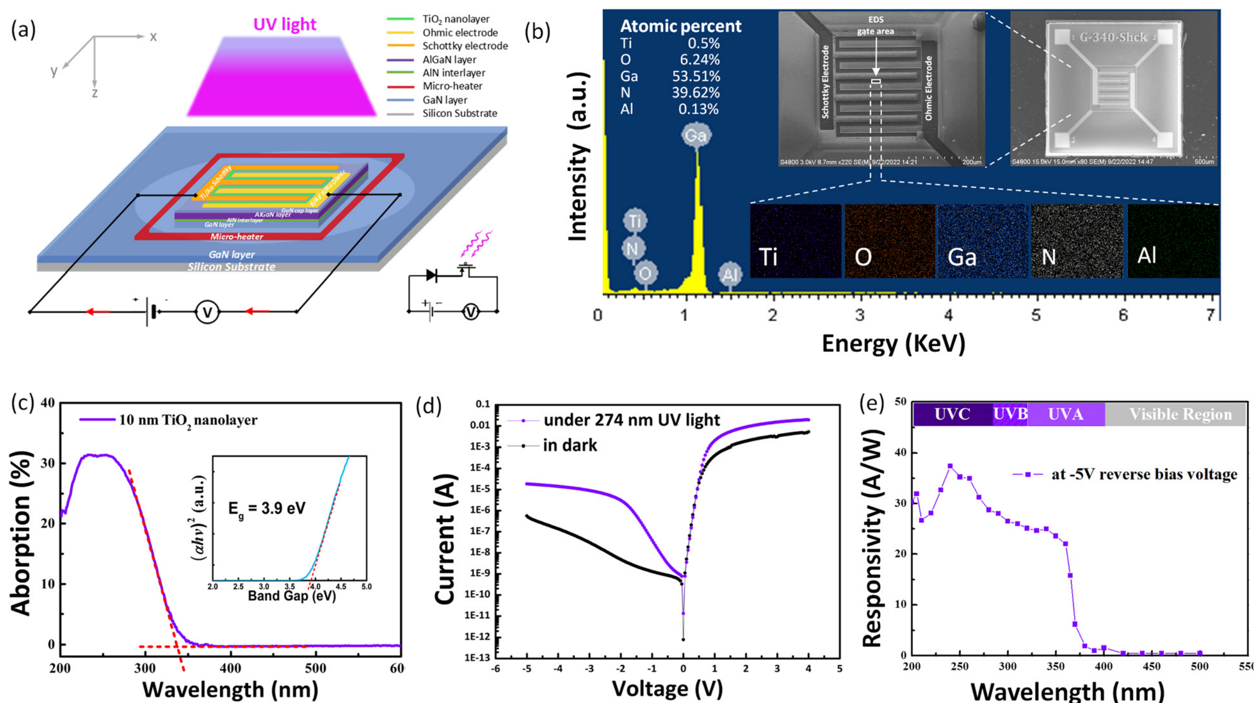

Fig. 1 (a) Schematic of the TiO_2/AlGaN/GaN heterostructure photodetector with a Schottky junction and the device model: the inset shows the device model of a 2DEG FET and a Schottky diode; (b) EDS spectra of the detector gate surface, the inset shows an SEM image of a single chip and distribution diagram of each element in the TiO_2 gate area; (c) absorption curve of a 10 nm TiO_2 nanolayer, the inset shows its bandgap; (d) *I–V* curve of the device in the dark state and under 274 nm UV light irradiation; (e) measured spectral response of the TiO_2/AlGaN/GaN heterostructure photodetector under −5 V reverse bias.

Published on 13 December 2022. Downloaded by Technische Universiteit Delft on 1/17/2023 8:23:20 AM.

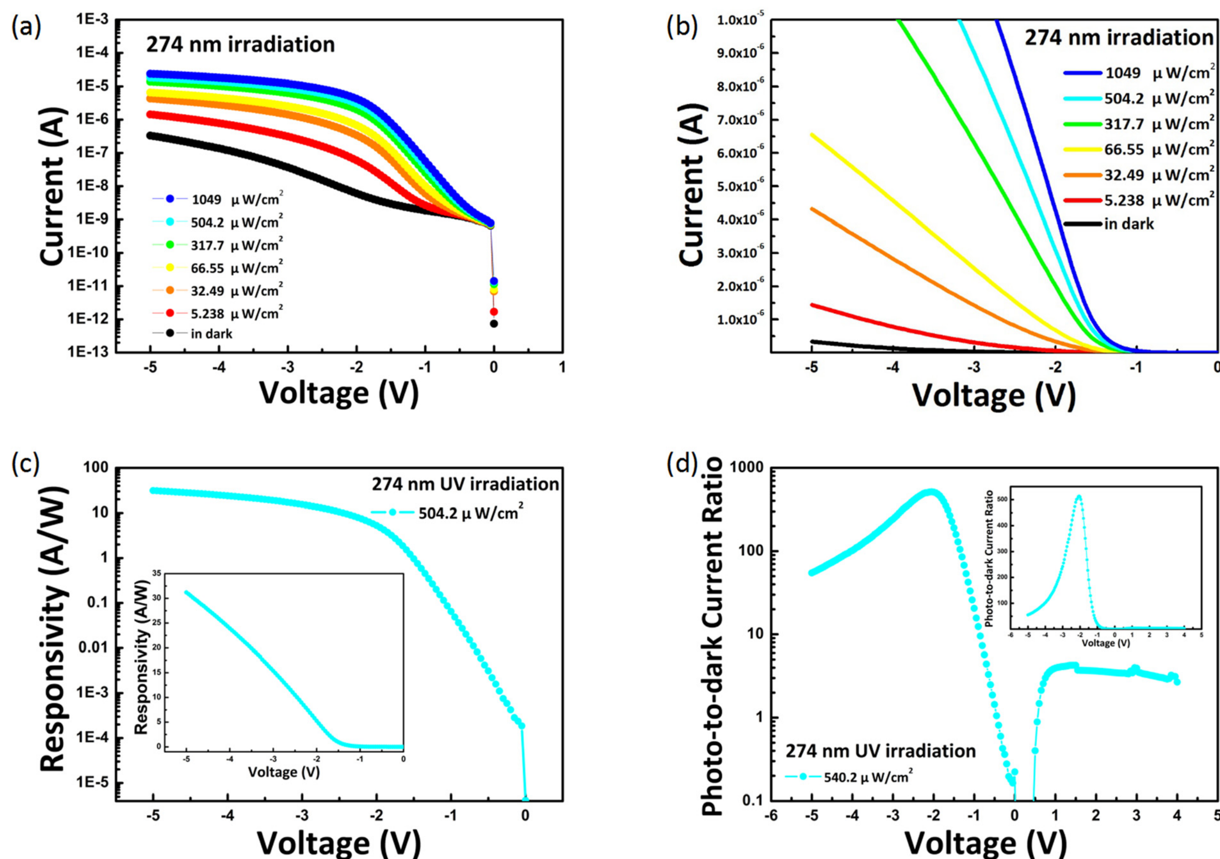

Fig. 2 *I–V* characteristics of the Schottky junction-based TiO_2/AlGaN/GaN heterostructure UV photodetector under 274 nm light illumination with different intensities of applied voltages ranging from −5 V to 0 V on (a) a semilogarithmic current scale and (b) a linear current scale; (c) the semilogarithmic responsivity under 274 nm illumination with an intensity of 504.2 μW cm^{-2} at applied voltages from −5 V to 0 V, the inset shows the linear scale; (d) the photo-to-dark current ratio of the detector under 274 nm illumination with an intensity of 504.2 μW cm^{-2} at applied voltages from −5 V to 4 V on a semilogarithmic scale, the inset shows the linear scale.

240 nm UV illumination, and a PDCR of 55.76 was observed. A sharp cutoff wavelength of the detector, defined as the ratio between the maximum responsivity and the natural constant ($e \approx 2.718$), is located at 365 nm.[38,39]

We systematically tested the photoelectric response characteristics of this Schottky junction-based TiO_2/AlGaN/GaN heterostructure UV photodetector. Fig. 2(a) shows the *I–V* curves of the photodetector in the dark and under 274 nm UV light illumination with intensities of 5.238 μW cm^{-2}, 32.49 μW cm^{-2}, 66.55 μW cm^{-2}, 317.7 μW cm^{-2}, 504.2 μW cm^{-2}, and 1049 μW cm^{-2}. A significant response is observed when the Schottky junction-based detector is irradiated by UV light of varying intensities at applied reverse voltages from −5 V to 0 V. The photocurrents increase as the light intensity increases. For example, as shown in Fig. 2(a) and (b), under −2 V reverse bias, the photocurrent reaches 6.03 nA, 59.57 nA, 340 nA, 678 nA, 2.014 μA, 3.083 μA, and 4.269 μA, when light intensities are of 5.238 μW cm^{-2}, 32.49 μW cm^{-2}, 66.55 μW cm^{-2}, 317.7 μW cm^{-2}, 504.2 μW cm^{-2}, and 1049 μW cm^{-2}, respectively in the dark. Interestingly, under 0 V bias, the current can be 1.69 pA, 6.97 pA, 7.93 pA, 11.49 pA, 13.33 pA, and 14.21 pA, with light intensities of 5.238 μW cm^{-2}, 32.49 μW cm^{-2}, 66.55 μW cm^{-2}, 317.7 μW cm^{-2}, 504.2 μW cm^{-2}, and 1049 μW cm^{-2}, respectively, indicating a self-powered working mode of this detector at 0 V bias, as shown in Fig. 2(a). Fig. 2(c) shows that the detector responsivity increases as the applied reverse voltages increase when the intensity of UV light remains constant. The responsivities are 0.064 A W^{-1}, 5.279 A W^{-1}, 15.38 A W^{-1}, 23.92 A W^{-1}, and 31.19 A W^{-1} when the reverse voltages are −1 V, −2 V, −3 V, −4 V, and −5 V, respectively, under 274 nm irradiation with an intensity of 504.2 μW cm^{-2}. On a linear scale, the inset of Fig. 2(c) shows that when the reverse bias voltage is greater than −1.5 V, the detector responsivity increases rapidly, indicating the transformation of the response mechanism. To better understand the characteristics and advantages of this Schottky junction–based structure, we plotted the PDCR, $(I_{photo} - I_{dark})/(I_{dark})$ of the detector under 274 nm illumination with an intensity of 504.2 μW cm^{-2} at applied voltages from −5 to 4 V on a semilogarithmic scale. As shown in Fig. 2(d), A PDCR of 5.1×10^2 was observed at −2 V bias, which is larger than the PDCR value at other voltages, both reverse and forward voltages, which could be attributed to the transformation of the detection mechanism at −2 V bias. The PDCR at the forward voltages is inferior to that at

 This journal is © The Royal Society of Chemistry 2023

Published on 13 December 2022. Downloaded by Technische Universiteit Delft on 1/17/2023 8:23:20 AM.

the reverse. Voltages due to the different response mechanisms at the reverse and forward voltages caused by the Schottky junction structure. The maximum PDCR value of the forwarding bias voltage is 4.27 at 1.5 V. Hence, the present TiO_2/AlGaN/GaN heterostructure UV detector shows higher PDCR and sensitivity at reverse bias than at the forward bias. Fig. 2(d) and the inset show the PCRD value on semilogarithmic and linear scales, respectively.

Fig. 3 shows the current–time (*I*–*t*) curves of the detector under 274 nm UV irradiation with a light intensity of 504.2 μW cm^{-2} at applied voltages from −0.7 to −2.8 V. When exposed to UV light, the photocurrent increases linearly as the reverse voltage increases, as shown in Fig. 3(a) and 2(b). The maximum photocurrents were 18.5 nA, 130 nA, 439 nA, 1.82 μA, 3.61 μA, 6.825 μA, 9.81 μA, and 11.77 μA for reverse voltages of −0.7 V, −1.0 V, −1.2 V, −1.5 V, −1.7 V, −2.0 V, −2.3 V, −2.5 V, and −2.8 V, respectively. Upon removing the UV illumination, the photocurrent slowly decays with a long recovery time of several minutes to several hours. The PPC effect has also been observed in this Schottky junction-based TiO_2/AlGaN/GaN heterostructure UV detector. However, through repeated measurements, the results indicate that the decay time was decreased under constant UV irradiation while the reverse bias voltage increased, as shown in Fig. 3(a) and (b). Fig. 3(b) illustrates the normalized *I*–*t* curves of the detector under 274 nm UV irradiation with a light intensity of 504.2 μW cm^{-2}. The photocurrent continuously increased slowly until the UV light of 274 nm was removed. Table 1 summarizes the rise time and the ratio of recovery current to peak photocurrent after removing UV light for 10 s and 100 s. The rise time (defined as the time required for the peak photocurrent to increase from 10% to 90%) ranges from 81.3 s to 52.6 s at applied voltages from −0.7 to −2.8 V. After removing UV light for 10 s, the recovery current decay from 85.1% to 35.2% of the peak photocurrent at applied voltages ranging from −0.7 to −2.8 V, respectively. After removing the UV light for 100 s, the decay of current is from 71.8% to 17.2% of the peak photocurrent. The slow response speed in this device is mainly caused by rich oxygen vacancies and many material defects in the TiO_2 nano layer. And the response time is strongly dependent on the surface roughness and resistance of the TiO_2 film. Fig. 3(c) presents the plot of recovery current to photocurrent ratio *versus* negative voltage, which could also support this phenomenon. Significantly, Fig. 3 shows that a higher reverse voltage results in a shorter decay time which begins to stabilize when the reverse bias exceeds −2 V, indicating a transformation of dominant response and recovery mechanism between negative bias −2 V and −2.3 V.

To further understand the response and recovery working principle of the Schottky junction-based TiO_2/AlGaN/GaN heterostructure UV detector, current conduction mechanisms were analyzed in detail using the measurement results. In this Schottky structure, three current conduction mechanisms were observed in this detector while the device was working at reverse bias voltages, including SE/TE, Poole–Frenkel (PF) emission, and Fowler–Nordheim (FN) tunneling under UV irradiation. Fig. 4(a) illustrates the schematic of the Schottky emission, PF emission, and FN tunneling in an energy band diagram of the detector. Fig. 4(b)–(d) presents the plots of the In(*J*) *versus* $E^{1/2}$, In(*J*/*E*) *versus* $E^{1/2}$, and In(*J*/E^2) *versus* E^{-1} curves, respectively. All the results were measured at room temperature (300 K).

The SE is a conduction mechanism that allows electrons in the metal to pass through the interface barrier to the dielectric if they obtain enough energy from thermal activation. The expression of the SE mechanism is as follows:[37,40,41]

$$J_{SE} = A^* T^2 \exp\left[-\frac{q\left(\phi_{SB} - \sqrt{qE/4\pi\varepsilon_r\varepsilon_0}\right)}{kT}\right], \qquad (1)$$

$$A^* = \frac{4\pi q k^2 m^*}{h^3} = \frac{120 m^*}{m_0}, \qquad (2)$$

where J is the current density; A^* is the effective Richardson constant; m and m_0 are the free electron effective mass and the electron effective mass in the AlGaN thin film; T and q are the absolute temperature and the electronic charge, E is the electric field; k and h are the Boltzmann's constant and the Planck's constant, respectively; ε_0 and ε_r are the vacuum and optical dielectric constants, respectively; and $q\,\phi_B$ is the Schottky barrier height. The original SB height ϕ_{SB} is determined by the work-function difference between the metal Ti and AlGaN layer interface, and the $q\,\phi_B$ is 1.83 eV in this photodetector. By fitting the In(*J*) − $E^{1/2}$ plots shown in Fig. 4(b), the linear

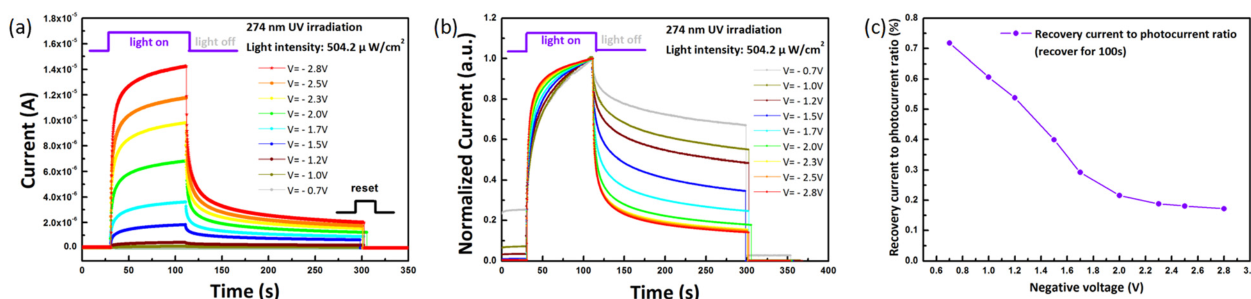

Fig. 3 *I*–*t* curves of the Schottky junction-based TiO_2/AlGaN/GaN heterostructure UV photodetector under 274 nm light illumination with an intensity of 504.2 μW cm^{-2} at applied voltages ranging from −0.7 to −2.8 V on (a) a linear current scale and (b) a normalized current scale; (c) Recovery current to photocurrent ratio *versus* negative voltage after removing UV light for 100 s.

Table 1 Rise time, ratio of the recovery current to photocurrent after the removal of UV light for 10 s and 100 s under 274 nm illumination with intensity of 504.2 μW cm^{-2}

Wavelength	274 nm UV illumination, 504.2 μW cm^{-2}								
Bias	−0.7 V	−1.0 V	−1.2 V	−1.5 V	−1.7 V	−2.0 V	−2.3 V	−2.5 V	−2.8 V
Rise time [s]	81.3	78.2	75.8	70.1	66.3	60.9	57.6	54.4	52.6
Recovery current to photocurrent ratio after the removal for 10 s [%]	85.1	78.3	71.9	61.4	49.8	40.5	35.8	35.8	35.2
Recovery current to photocurrent ratio after the removal for 100 s [%]	71.8	60.6	53.8	39.9	29.2	21.6	18.8	18.1	17.2

Published on 13 December 2022. Downloaded by Technische Universiteit Delft on 1/17/2023 8:23:20 AM.

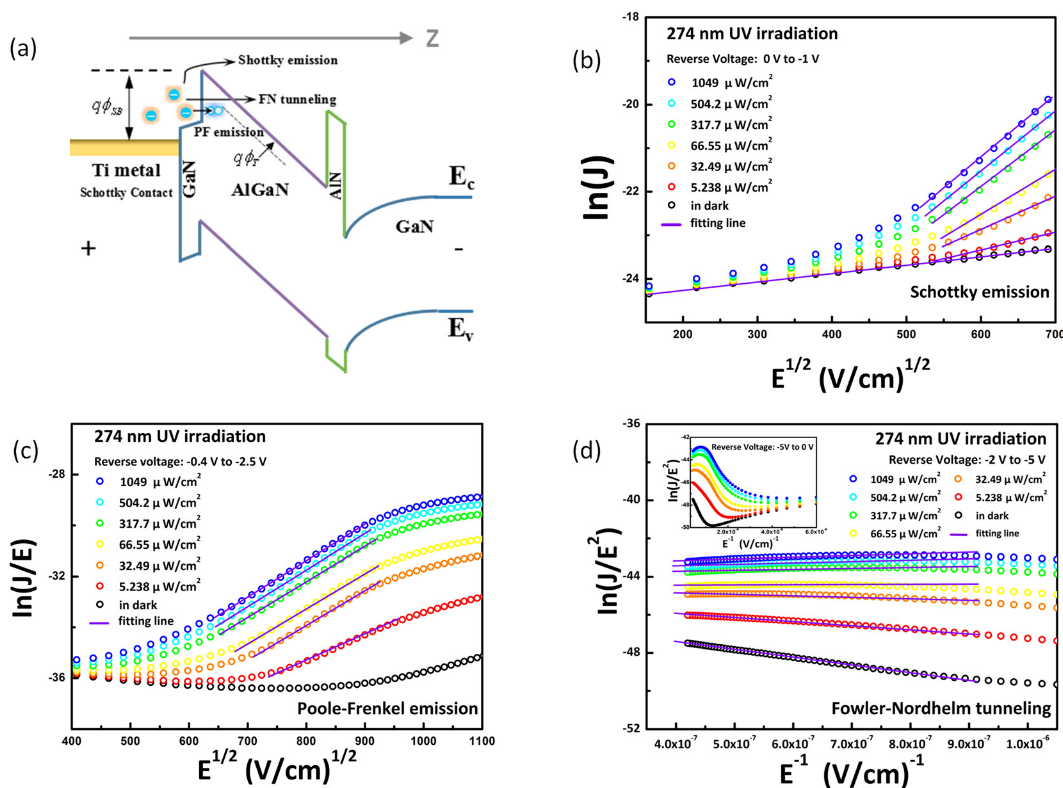

Fig. 4 (a) Schematic of Schottky emission, PF emission, and FN tunneling in an energy band diagram of Schottky junction–based TiO_2/AlGaN/GaN heterostructure UV detector. (b) SE mechanism: ln(J) *versus* $E^{1/2}$ plots of the detector at a reverse voltage from 0 to −1 V, (c) PF emission mechanism: ln(J/E) *versus* $E^{1/2}$ at a reverse voltage from −0.25 to −3.25 V, and (d) FN tunneling mechanism: ln(J/E^2) *versus* E^{-1} under 274 nm UV irradiation at a reverse voltage from −2 to −5 V, the inset shows the curves within a voltage range from −0.5 to −5 V.

reverse bias voltage ranges from 0 to −1 V, indicating that the Schottky emission mechanism dominates the Schottky junction–based detector for reverse injection in the low electric field region.

The PF emission is a conduction mechanism that the thermally excited electrons may emit from metal–AlGaN/GaN Schottky interface traps into the conduction band of the AlGaN layer to form a leakage current. The expression of the PF emission mechanism is as follows:[37,40,42]

$$J_{\rm PF} = CE\exp\left[\frac{-q\left(\phi_{\rm T} - \sqrt{qE/\pi\varepsilon_0\varepsilon_{\rm AlGaN}}\right)}{kT}\right], \qquad (3)$$

where C is a constant and $q\,\phi_{\rm T}$ and $\varepsilon_{\rm AlGaN}$ refer to the trap energy level and dielectric constant of the AlGaN layer. Fig. 4(c) depicts a plot of In(J/E) − $E^{1/2}$ for the theoretical expression of PF emission.

The results and fitting line show good linear behavior in the reverse voltage from −1 V to −2 V bias, indicating the existence of PE emission while the detector is irradiated by UV light with different densities at this reverse voltage region. The thickness of the AlGaN dielectric layer and the area of Ti/AlGaN Schottky contact in this UV detector are 21 nm and 0.2465 mm^2, respectively. According to the fitting lines in Fig. 4(c) and the slope $\frac{\sqrt{q^3/\pi\varepsilon_0\varepsilon_{\rm AlGaN}}}{kT}$, the value of $\varepsilon_{\rm AlGaN}$ can be extracted to be about 9.1, which was consistent with the dielectric constant ε of Al-doping GaN materials. For the PF emission, the trap energy height can be analyzed by the intercept of fitting lines. According to the intercept expression = In $B - \frac{q\phi_{\rm T}}{kT}$ and plots of

 This journal is © The Royal Society of Chemistry 2023

Published on 13 December 2022. Downloaded by Technische Universiteit Delft on 1/17/2023 8:23:20 AM.

$\ln(J/E) - E^{1/2}$, the trapped energy level $q\,\phi_T$ in the AlGaN layer can be extracted to be about 0.74 eV.

The photodetector exhibits an FN tunneling mechanism in the higher reverse bias voltage regions. The expression of the FN tunneling mechanism is as follows[37,40,41]

$$J_{FN} = \frac{q^3E^2}{8\pi hq\phi_{SB}}\exp\left[\frac{-8\pi\phi_{SB}^{3/2}\sqrt{2qm_T^*}}{3hE}\right], \quad (4)$$

where m_T^* is the tunneling effective mass in the dielectric AlGaN layer and the other notations are the same as defined earlier. For the FN tunneling theoretical expression (4), a plot of $\ln(J/E^2) - E^{-1}$ is illustrated in Fig. 4(d). According to the fitting line, a good linear behavior of $\ln(J/E^2)$ *versus* E^{-1} is shown while the photodetector was irradiated under 274 nm UV light with different densities in the reverse voltage from −2.3 V to −5 V bias. Without UV light illumination, the detector also observed the FN tunneling while the reverse voltage was larger than −2.3 V in the dark state. The slopes of the fitting curves for the detector with increasing UV light densities are regular and stable. The inset of Fig. 4(d) shows $\ln(J/E^2) - E^{-1}$ plots in the reverse voltage ranging from 0 to −5 V. Notably, the linear behavior of the FN tunneling mechanism appeared only when the reverse bias was larger than −2.3 V, indicating that this Schottky junction-based TiO_2/AlGaN/GaN heterostructure detector is consistent with the FN tunneling mechanism in the high reverse biases or high electric fields on the Ti/AlGaN Schottky interface. The expression of width at the depletion layer formed at the SB area is as follows:

$$W_D = \sqrt{\frac{2\varepsilon_S}{qN_D}\left(V_{bi} - V - \frac{kT}{q}\right)}, \quad (5)$$

where V_{bi} is the built-in potential and $V_{bi} = \phi_{SB} - (E_c - E_f)$. Under UV illumination, we can conclude that the current passing through the Schottky contact is very sensitive to the Schottky barrier height and barrier width under a reverse bias voltage. The reverse bias voltage and UV light illumination can alter the local electric-field distribution and carrier concentration near the SB area, affording the variation of the SB width and height.

Based on the above analysis of SE, PF emission, and FN tunneling, it can be concluded that as the reverse bias increases, the dominant working principle of the photodetector shifts from SE to PF emission and FN tunneling mechanism. As shown in Fig. 2(d) and 3(b), the peak PDCR value and the stable recovery time appear at about −2.3 V reverse bias owing to the transformation of the working mechanism with increasing the reverse voltage. In the *I–V* curves, when the reverse voltage is greater than −2 V, the current of the detector begins to rapidly increase in a dark state due to FN tunneling, as shown in Fig. 2(a) and Fig. S3 (ESI†).

Fig. 5(a) summarizes the dominant current conduction mechanisms of the detector under UV illumination at the negative bias of 0 to 5 V. Fig. 5(b)–(d) illustrate the schematic of the energy band diagrams of the photodetector. In Fig. 5(c),

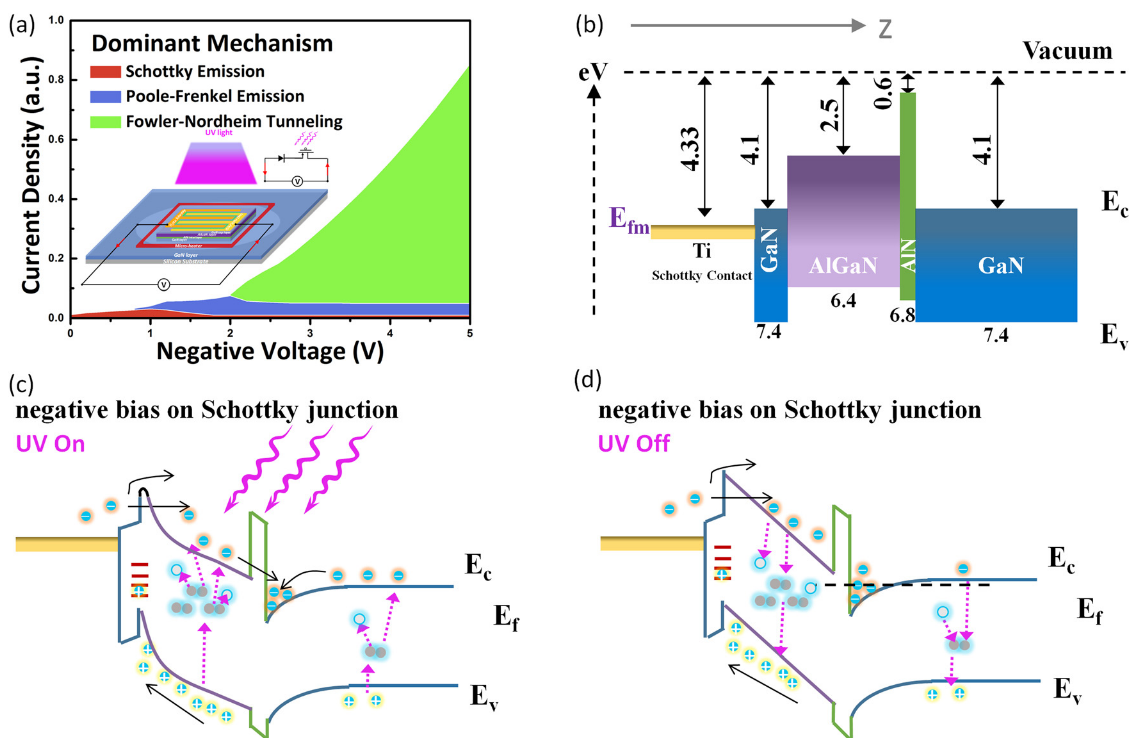

Fig. 5 (a) An overview of the dominant current conduction mechanisms of the detector under UV illumination in the negative 0 to 5 V region. (b) A schematic illustration of the energy band diagrams describes the TiO_2/AlGaN/GaN heterostructure photodetector with the Schottky junction. (c) Under UV illumination and (d) upon removal of UV illumination.

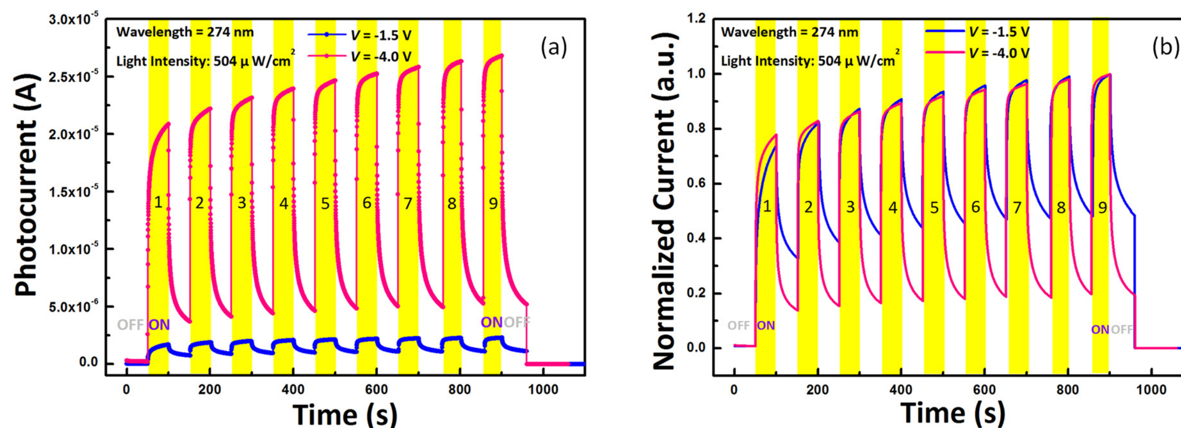

Fig. 6 The transient photocurrent response of the Schottky junction-based TiO_2/AlGaN/GaN heterostructure photodetector under 274 nm UV illumination at negative bias $V = -1.5$ V and $V = -4$ V. (a) Nine cycles with UV light intensity of 504 μW cm^{-2} on a linear current scale and (b) on a normalized current scale.

the photogenerated electrons in the TiO_2 floating gate nanolayer and AlGaN/GaN heterostructure drift toward the 2DEG channel under UV illumination and negative bias voltage, increasing the concentration of 2DEG and the current between source and drain electrodes. Meanwhile, the photogenerated holes in the AlGaN layer drift toward the Ti/AlGaN Schottky junction surface driven by reverse bias voltage (built-in electric field) and get captured at the interface centers or the deep centers. The holes trapping in the Schottky surface can induce height reduction of the Schottky barrier and width narrowing in the depletion region, which will enhance the reverse leakage current by SE, PF emission, or FN tunneling mechanism. After removing the UV illumination, a long recovery time was observed in the TiO_2/AlGaN/GaN Schottky-based ultraviolet detector, as shown in Fig. 3 and 5(d). The PPC effect in this device is mainly caused by three physical phenomena. Firstly, GaN materials contain many defects, and the deep-level energy barrier can delay the recombination of photogenerated carriers, resulting in a persistent photoconductivity effect. Secondly, once the UV illumination is removed, the photogenerated electrons that flow into the 2DEG channel cannot immediately recombine with excited holes in TiO_2/AlGaN/GaN materials, inducing a longer recovery time. Thirdly, even after the UV light is turned off, the trapping holes in the TiAu/AlGaN Schottky junction surface are still maintained due to the electric field, causing a persistent leakage current.[43–45]

Fig. 6(a)–(b) shows the curves of transient response photocurrent *versus* time for the Schottky junction-based TiO_2/AlGaN/GaN heterostructure photodetector under 274 nm UV illumination with a light intensity of 504 μW cm^{-2} at negative bias $V = -1.5$ V and $V = -4$ V. The UV light was kept on and off for 50 s each. In Fig. 6(a), the curves indicate that under −1.5 V and −4 V bias voltages, when the detector is exposed to UV light, the response photocurrent varies according to the applied negative bias. As shown in Fig. 6(a) and 2(c), the photocurrent and responsivity at −4 V considerably exceed that at −1.5 V. After nine cycles, the photocurrent of the detector maintains consistency and repeatability. However, the photocurrent is sustained, gradually increasing in each cycle under UV light, which may be attributed to the photoresponse characteristics of TiO_2 materials. As shown in Fig. 3, the higher the reverse bias voltage applied, the shorter the decay time. The same phenomenon is depicted on a normalized current scale shown in Fig. 6(b); the measurement results show that the transient response and recovery of the detector have good repeatability at different applied negative voltages after nine cycles.

Table 2 compares various Schottky junction-based photodetectors with different device structures and current

Table 2 Comparison among various photodetectors with different current conduction mechanisms

Photodetector device structure	Wavelength (nm)	Current conduction mechanism	Peak R (A W^{-1}) @RT	Peak PDCR @RT	Ref.
TiO_2/AlGaN/GaN heterostructure with Schottky junction	200–365	SE to PF and FN	37.396@−5 V	5.1×10^2	This work
ZnO NWs with Schottky contacts	UV	TED	—	—	30
β-Ga_2O_3 with M-S Schottky contacts	200–255	TFE	0.21@8 V	4×10^4	35
BLG/GaAs Schottky junction with AlO_x interface layer	800–900	SE/TE	0.005	10^5	46
Multilayer p–i–n α-Se avalanche structure	—	SE, PF	—	—	47
MSM InGaN with CaF_2 insulator	338	TFE, TAT	10.4@2 V	10^5	48
MSM-ε-Ga_2O_3	200–270	TFE, PF	230@6 V	1.2×10^5	49
High Al-content $Al_{0.6}Ga_{0.4}N$ MSM structure	200–255	TFE, PF	0.51@10 V	—	50
n-Si/TiO_2 nanorod array heterojunction	400–600	SE	>0.3@−4 V	>2	51

Published on 13 December 2022. Downloaded by Technische Universiteit Delft on 1/17/2023 8:23:20 AM.

This journal is © The Royal Society of Chemistry 2023

Published on 13 December 2022. Downloaded by Technische Universiteit Delft on 1/17/2023 8:23:20 AM.

conduction mechanisms. Here, the SE, PF, and FN mechanisms were only observed simultaneously, indicating that the detector can exhibit different dominant mechanisms under different reverse bias conditions according to specific application requirements. Meanwhile, the TiO_2/AlGaN/GaN heterostructure photodetector with Schottky junction has a high responsivity and PDCR value. Furthermore, the metal-oxide/AlGaN/GaN heterostructure can easily change the UV response spectrum region by selecting metal-oxide gate nanoscale materials, as reported in our previous publications.[21,22]

Conclusions

A novel integrated photodetector is demonstrated based on a TiO_2/AlGaN/GaN and Ti/AlGaN Schottky junction. The device is an ultraviolet detector with high performance and stability, which is demonstrated using a TiO_2 nanolayer as UV sensitive materials, AlGaN/GaN 2DEG FET as the signal amplification structure, and a Ti/AlGaN Schottky diode as the dominant current conduction structure. Three working mechanisms at different bias voltages, including SE, PF emission, and FN tunneling, aid in selecting different working modes according to specific application requirements. Notably, this Schottky junction-based detector obtains a high PDCR value, which indicates that the devices have a higher sensitivity than a traditional metal-oxide/AlGaN/GaN heterostructure photodetector. Systematically analyzing and discussing the current conduction mechanisms for the Schottky contact of the UV detector herein can provide a reference for future advanced ultraviolet detection technology.

Conflicts of interest

There are no conflicts to declare.

Acknowledgements

Teng Zhan and Jianwen Sun contributed equally to this paper. This work was supported by the National Key R&D Program of China (2021YFB3601000, 2021YFB3601004) and the Chinese Academy of Sciences, the National Key R&D Program (2019YFA0707002) and Tsinghua University. The authors would like to thank Gang Sun and Suxia Zhang from Zolix Instrument Co., Ltd for the spectral response testing.

Notes and references

1 W. Zheng, F. Huang, R. Zheng and H. Wu, *Adv. Mater.*, 2015, **27**, 3921–3927.
2 Y. Zou, Y. Zhang, Y. Hu and H. Gu, *Sensors*, 2018, **18**, 2072.
3 J. Xu, W. Zheng and F. Huang, *J. Mater. Chem. C*, 2019, **7**, 8753–8770.
4 R. Z. Yuan and J. S. Ma, *China Commun.*, 2016, **13**, 63–75.
5 C. Xie, X. Lu, X. Tong, Z. Zhang, F. Liang, L. Liang, L. Luo and Y. Wu, *Adv. Funct. Mater.*, 2019, **29**, 180600.
6 D. B. Li, K. Jiang, X. J. Sun and C. Guo, *Adv. Opt. Photonics*, 2018, **10**, 43–110.
7 W. Zhang, J. Xu, W. Ye, Y. Li, Z. Qi, J. Dai, Z. Wu, C. Chen, J. Yin and J. Li, *Appl. Phys. Lett.*, 2015, **106**, 021112.
8 P. E. Malinowski, J. Y. Duboz, P. De Moor, K. Minoglou, J. John, S. M. Horcajo, F. Semond, E. Frayssinet, P. Verhoeve, M. Esposito, B. Giordanengo, A. BenMoussa, R. Mertens and C. V. Hoof, *Appl. Phys. Lett.*, 2011, **98**, 141104.
9 R. Dahal, T. M. Al Tahtamouni, J. Y. Lin and H. X. Jiang, *Appl. Phys. Lett.*, 2007, **91**, 243503.
10 W. Y. Kong, G. A. Wu, K. Y. Wang, T. F. Zhang, Y. F. Zou, D. D. Wang and L. B. Luo, *Adv. Mater.*, 2016, **28**, 10725–10731.
11 Y. Li, T. Tokizono, M. Liao, M. Zhong, Y. Koide, I. Yamada and J. J. Delaunay, *Adv. Funct. Mater.*, 2010, **20**, 3972–3978.
12 X. Chen, F. Ren, S. Gu and J. Ye, *Photonics Res.*, 2019, **7**, 381–415.
13 R. Zou, Z. Zhang, Q. Liu, J. Hu, L. Sang, M. Liao and W. Zhang, *Small*, 2014, **10**, 1848–1856.
14 C. Xie, X. Lu, Y. Liang, H. Chen, L. Wang, C. Wu, D. Wu, W. Yang and L. Luo, *J. Mater. Sci. Technol.*, 2021, **72**, 189–196.
15 W. Zheng, R. Lin, Z. Zhang and F. Huang, *ACS Appl. Mater. Interfaces*, 2018, **10**, 27116–27123.
16 M. Sajjad, W. M. Jadwisienczak and P. Feng, *Nanoscale*, 2014, **9**, 4577–4582.
17 Y. Peng, J. Lu, X. Wang, W. Ma, M. Que, Q. Chen, F. Li, X. Liu, W. Gao and F. C. Pan, *Nano Energy*, 2022, **94**, 106945.
18 G. Liu, H. Chen, S. Lu, L. Liu, X. Xu, L. Shi, B. Chen, B. Guo, P. Shen, Y. Cai, H. Zhang, Y. Tang, A. M. Soomro, F. Xu, X. Chen, T. Zheng, J. Li, S. Li, D. Cai and J. Kang, *Small*, 2022, **18**, 2200563.
19 Z. He, Q. Liu, H. Hou, F. Gao, B. Tang and W. Yang, *ACS Appl. Mater. Interfaces*, 2015, **7**, 10878–10885.
20 Z. Hai, M. K. Akbari, C. Y. Xue, H. Y. Xu, L. Hyde and S. Zhuiykov, *Appl. Surf. Sci.*, 2017, **405**, 169–177.
21 J. Sun, T. Zhan, Z. Liu, J. Wang, X. Yi, P. M. Sarro and G. Zhang, *Opt. Express*, 2019, **27**, 36405–36413.
22 J. Sun, S. Zhang, T. Zhan, Z. Liu, J. Wang, X. Yi, J. Li, P. M. Sarro and G. Zhang, *J. Mater. Chem. C*, 2020, **8**, 5409–5416.
23 L. Hu, J. Yan, M. Liao, L. Wu and X. Fang, *Small*, 2011, **7**, 1012–1017.
24 H. Chen, L. Hu, X. Fang and L. Wu, *Adv. Funct. Mater.*, 2012, **22**, 1229–1235.
25 X. Li, C. Gao, H. Duan, B. Lu, X. Pan and E. Xie, *Nano Energy*, 2012, **1**, 640–645.
26 Y. Gao, J. Xu, S. Shi, H. Dong, Y. Cheng, C. Wei, X. Zhang, S. Yin and L. Li, *ACS Appl. Mater. Interfaces*, 2018, **10**, 11269–11279.
27 L. Sang, M. Liao, Y. Koide and M. Sumiya, *Appl. Phys. Lett.*, 2011, **99**, 031115.
28 P. F. Satterthwaite, A. S. Yalamarthy, N. A. Scandrette, A. Newazand and D. G. Senesky, *ACS Photonics*, 2018, **5**, 4277–4282.
29 W. Xu, Y. Shi, F. Ren, D. Zhou, L. Su, Q. Liu, L. Cheng, J. Ye, D. Chen, R. Zhang, Y. Zheng and H. Lu, *Photonics Res.*, 2019, **7**, B48–B54.

Published on 13 December 2022. Downloaded by Technische Universiteit Delft on 1/17/2023 8:23:20 AM.

30 Y. Hu, J. Zhou, P. H. Yeh, Z. Li, T. Y. Wei and Z. L. Wang, *Adv. Mater.*, 2010, **22**, 3327–3332.
31 Y. Luo, X. Yan, J. Zhang, B. Li, Y. Wu, Q. Lu, C. Jin, X. Zhang and X. Ren, *Nanoscale*, 2018, **10**, 9212–9217.
32 Z. Zhang, Q. L. Liao, X. H. Zhang, G. J. Zhang, P. F. Li, S. N. Lu, S. Liu and Y. Zhang, *Nanoscale*, 2015, **7**, 1796.
33 Y. An, A. Behnam, E. Pop and A. Ural, *Appl. Phys. Lett.*, 2013, **102**, 013110.
34 W. Jiang, T. Zheng, B. Wu, H. Jiao, X. Wang, Y. Chen, X. Zhang, M. Peng, H. Wang, T. Lin, H. Shen, J. Ge, W. Hu, X. Xu, X. Meng, J. Chu and J. Wang, *Light-Sci.: Appl.*, 2020, **9**, 160.
35 Y. Xu, X. Chen, D. Zhou, F. Ren, J. Zhou, S. Bai, H. Lu, S. Gu, R. Zhang, Y. Zheng and J. Ye, *IEEE T. Electron. Dev.*, 2019, **66**, 2276–2281.
36 L. Wang, M. Lu, X. Wang, Y. Yu, X. Zhao, P. Lv, H. Song, X. Zhang, L. Luo, C. Wu, Y. Zhang and J. Jie, *J. Mater. Chem. A*, 2013, **1**, 1148.
37 Q. Fan, C. Ma, C. Ma, R. Lu, S. Cheng and M. Liu, *Appl. Phys. Lett.*, 2020, **116**, 192902.
38 B. Zhao, F. Wang, H. Chen, L. Zheng, L. Su, D. Zhao and X. Fang, *Adv. Funct. Mater.*, 2017, **27**, 1700264.
39 Y. C. Chen, Y. J. Lu, C. N. Lin, Y. Z. Tian, C. J. Gao, L. Dong and C. X. Shan, *J. Mater. Chem. C*, 2018, **6**, 5727–5732.
40 F. C. Chiu, *Adv. Mater. Sci. Eng.*, 2014, 578168.
41 D. Wang, G. He, L. Hao, J. Gao and M. Zhang, *J. Mater. Chem. C*, 2019, **7**, 1955.
42 A. Paskaleva, A. J. Bauer, M. Lemberger and S. Zucher, *J. Appl. Phys.*, 2004, **95**, 5583.
43 H. Zhou, L. Cong, J. Ma, B. Li, H. Xu and Y. Liu, *Chin. Phys. B*, 2021, **30**, 126104.
44 W. Zheng, R. Lin, D. Zhang, L. Jia, X. Ji and F. Huang, *Adv. Opt. Mater.*, 2018, **6**, 1800697.
45 S. Li, J. Yue, X. Ji, C. Lu, Z. Yan, P. Li, D. Guo, Z. Wu and W. Tang, *J. Mater. Chem. C*, 2021, **9**, 5437.
46 L. Luo, H. Hu, X. Wang, R. Lu, Y. Zou, Y. Yu and F. Liang, *J. Mater. Chem. C*, 2015, **3**, 4723.
47 L. T. T. Ho, A. Mukherjee, D. Vasileska, J. Akis, J. Stavro, W. Zhao and A. H. Goldan, *ACS Appl. Electron. Mater.*, 2021, **3**, 3538–3546.
48 L. Sang, M. Liao, Y. Koide and M. Sumiya, *Appl. Phys. Lett.*, 2011, **98**, 103502.
49 Y. Qin, L. Li, X. Zhao, G. S. Tompa, H. Dong, G. Jian, Q. He, P. Tan, X. Hou, Z. Zhang, S. Yu, H. Sun, G. Xu, X. Miao, K. Xue, S. Long and M. Liu, *ACS Photonics*, 2020, **7**, 812–820.
50 Y. Gu, G. Yang, A. Danner, D. Yan, N. Lu, X. Zhang, F. Xie, Y. Wang, B. Hua, X. Ni, Q. Fan, X. Gu and G. Chen, *IEEE T. Electron. Dev.*, 2020, **67**, 160–165.
51 T. Ji, Q. Liu, R. Zou, Y. Sun, K. Xu, L. Sang, M. Liao, Y. Koide, L. Yu and J. Hu, *Adv. Funct. Mater.*, 2016, **26**, 1400–1410.

 This journal is © The Royal Society of Chemistry 2023